

Article

A Period Energy Method for Demagnetization Detection in Surface Permanent Magnet Motors with Search Coils

Wen Huang , Junquan Chen, Wu Su, Haitao Liu , Ke Lv and Jinghua Hu *

National Key Laboratory of Electromagnetic Energy, Naval University of Engineering, Wuhan 430030, China; wenhuang@stu.xjtu.edu.cn (W.H.)

* Correspondence: hujinghua23@nue.edu.cn

Abstract: Irreversible demagnetization of permanent magnets (PMs) in PM synchronous motors (PMSMs) degrades the performance and efficiency of a machine and its drive system. There are numerous fault diagnosis methods for detecting demagnetization under steady-state conditions. However, only a few works could be found on fault diagnosis under dynamic conditions, whereas the dynamic operation of a motor is a very common scenario, e.g., electric vehicles. The voltage and current signal-based traditional fault detection method is not only affected by the structure of the motor, but it also becomes complicated to extract signals involving fault characteristics. Hence, this paper proposes a search coil-based online method for detecting demagnetization faults in PMSMs under dynamic conditions, which are not affected by the motor structure. To gather the flux of the stator tooth, flexible Printed circuit board (FPCB) search coils are positioned at the stator slot. The search coil is made up of two branches that are one pole apart and arranged in reverse sequence. In this installation option, the output signal in the fault state cannot be eliminated, and the output signal in the health state is zero. This paper defines only that characteristic value related to the position angle of the rotor. Further, the aim was to simultaneously eliminate the influence of elements like the search coil installation error and the inherent dispersion of the permanent magnet on the detection results. To characterize the fault degree, the measurement differential between the health state and the fault state is further integrated according to a predetermined angle range. Last but not least, speed-independent detection of individual permanent magnet demagnetization faults is possible using rotor position and stator tooth flux. A six-phase PMSM was used in experiments to show the efficiency of the suggested approach. The findings of the experiment demonstrate that the suggested strategy may precisely ascertain when a defect will occur.

Keywords: demagnetization; permanent magnet synchronous motor; dynamic conditions; search coils



Citation: Huang, W.; Chen, J.; Su, W.; Liu, H.; Lv, K.; Hu, J. A Period Energy Method for Demagnetization Detection in Surface Permanent Magnet Motors with Search Coils.

Electronics **2023**, *12*, 3514. <https://doi.org/10.3390/electronics12163514>

Academic Editors: Jose Luis Calvo-Rolle and Francisco Zayas-Gato

Received: 14 July 2023

Revised: 11 August 2023

Accepted: 16 August 2023

Published: 19 August 2023



Copyright: © 2023 by the authors. Licensee MDPI, Basel, Switzerland. This article is an open access article distributed under the terms and conditions of the Creative Commons Attribution (CC BY) license (<https://creativecommons.org/licenses/by/4.0/>).

1. Introduction

Permanent magnet synchronous motors (PMSMs) have found widespread use in industrial production, electric vehicles, aerospace, and other industries thanks to the development of high-quality rare-earth permanent magnetic materials [1,2] and power electronics technology [3,4]. Generally, the use of PMs in electrical machines has some advantages, such as fewer losses, more torque (power) per volume, better dynamic performance, simple structure, and simple maintenance [5]. These advantages are reinforced by the continuous development of materials technology [6–9]. In order to maintain such advantages in different applications, the operating condition of PMSMs must be monitored. Early and correct diagnosis of faults helps in improving the reliability and safety of a system. Due to this, numerous studies have been conducted to address problems, including demagnetization, electrically short/open circuits, static/dynamic eccentricity, and bearing faults [10,11]. Demagnetization is classified into two groups: reversible demagnetization and irreversible demagnetization. Reversible demagnetization is induced by a control that weakens the field, while irreversible demagnetization means permanently weakened

magnets. PMs may also get demagnetized as a result of mechanical, thermal, and aging processes while operating at a high temperature, which is the most frequent reason for PM failures [12]. Demagnetization significantly degrades the characteristics and efficiency of the motor as a result of the machine's decreased output torque. Demagnetized PMSMs require a larger current than a typical machine to maintain the same torque, but the increased current also raises the machine's temperature and copper losses. It is well known that a high temperature may produce very severe irreversible demagnetization [13,14]; therefore, it is crucial to research PMSM demagnetization defect diagnostics. Both steady-state and dynamic-state studies on demagnetization flaws in permanent magnets are currently conducted [5].

Flux analysis is the most direct method for detecting demagnetization faults of PMs, where partial and uniform demagnetization can be easily detected by directly measuring the magnetic flux with a Gaussian meter [15] or hall sensor [16]. However, this method requires disassembling the motor, so it is not a suitable method for online detection of demagnetization faults. Wiehan [17], Subhadeep [18], Satish [19], and Amir [20] employed the machine model to indirectly acquire flux information via a parameter estimate approach to tackle this problem. However, because of this method's high reliance on motor parameters, changing the motor parameters under various operating circumstances may significantly alter the results of the observations.

Stator current analysis is currently the most popular non-invasive method for detecting demagnetization faults of PMs because it is inescapably necessary to collect the stator current during the motor control process, which means that no additional sensors are required to obtain the signal to be analyzed [21–24]. The harmonic components in Equation (1) will manifest in the current spectrum when the demagnetization failure in the permanent magnet occurs. For non-stationary operating situations, several complicated time–frequency analysis techniques are suggested, including the short-time Fourier transform (STFT) [25], wavelet transform (WT) [26,27], and Hilbert–Huang transform (HHT) [14,28]. It is important to note that each series coil in a PMSM with symmetrical concentrated windings exhibits harmonic induced voltage components, but these harmonics cancel out throughout the entire winding [29].

$$f_{demag} = f_e \left(1 \pm \frac{k}{p} \right) \quad (1)$$

Information such as torque and vibration can also be used to check whether there is any demagnetization fault [30–33]. Although such methods can generally give accurate results, they often require expensive and complex sensors to support them.

The signal injection-based parameter estimation method can avoid the influence of motor parameters on the observation results. It can also consider non-ideal factors, such as saturation. Hong [34] injected current into the D-axis to detect the change in its inductance under saturation, where the demagnetization fault of the PM was detected and distinguished from the eccentric fault. This method can achieve significant advantages if the operating point of the motor comes at the knee point of the demagnetization curve of the PM; otherwise, a large current is required to saturate the core, which limits the application scenarios of this approach. With the further improvement in computing power, many intelligent algorithm-based methods have been proposed for detecting demagnetization faults [3,12,35]. Although the detection accuracies of these methods are increasing, a large amount of data accumulation and calculation are necessary prerequisites for accurate detection.

The approach, developed on the basis of search coils (SCs) for directly observing the change in the magnetic field of the motor, has received the attention of many scholars in spite of being an invasive detection method [36,37]. Da [37] used low-frequency components of the voltage signal of an SC so that its feature was not obvious, and the operating condition of the motor could influence the diagnosis.

On the basis of the above, an SC-based novel method for diagnosing demagnetization faults of PMSMs is proposed in this article. Search coils are made of flexible PCB in a way

enabling an increase in the number of turns if the full rate of the slot is certain, where increased turns makes it easier to detect fault signals. Similar to the conventional method, flux information in the search coil is used to diagnose the demagnetization fault. In this paper, it is innovatively proposed to transform the time domain information obtained by the search coil into the angle domain information for further analysis. Through the conversion strategy mentioned above, the proposed method is not only suitable for the steady state operation of the motor but also can achieve a good fault detection effect in the dynamic operation of the motor. Further, in order to describe the fault degree more intuitively, the paper defines “periodic energy”, which is directly proportional to the fault degree from both theoretical analysis and experimental verification. In addition, compared with Fourier decomposition and other spectral analysis methods commonly used in traditional fault detection methods, the proposed method only needs to perform a simple summation calculation of the measured signal, and the minimal calculation amount makes it easier to integrate the method into the motor system.

The rest of this article is organized as follows: The proposed method is in-depth and theoretically explored in Section 2; the proposed fault detection approach is validated through simulation and experiments in Section 3; Section 4 discusses the existing research methods and the proposed schemes; and Section 5 concludes this article.

2. Materials and Methods

In this paper, the stator of the motor is considered to be in a healthy state. So, only the effect of the rotor part on the search coil is taken into account. The information about a fault is obtained by detecting the response of the voltage induced in the coil. So, the accurate calculation of the air-gap magnetic field is an important step in the theoretical analysis. In this section, the proposed method is theoretically analyzed in detail. In order to calculate the air-gap magnetic field, first of all, the permanent magnet is made equivalent to a series of symmetric current-carrying coils by means of surface current equivalence. Then, it is transformed into a conventional current-carrying coil calculation model by correcting the Carter coefficient. Finally, in order to consider the influence of the actual motor fluting effect, the specific permeability function is calculated by modifying the ideal air-gap magnetic field by using conformal transformation. The calculation process of theoretical analysis is shown in Figure 1.

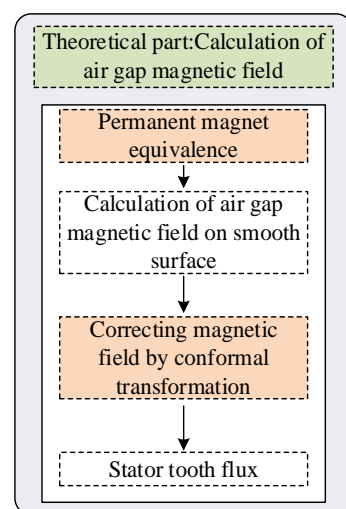


Figure 1. Calculation flow of stator tooth flux considering slot effect.

2.1. Magnetic Pole Surface Current Equivalence

A surface-mounted permanent magnet synchronous motor with sinusoidal pole clipping serves as the paper’s prototype. The shape of the permanent magnet is shown in

Figure 2 represented by red line. It can be made equivalent to the surface current depicted in Figure 2 for a permanent magnet that is parallel magnetized.

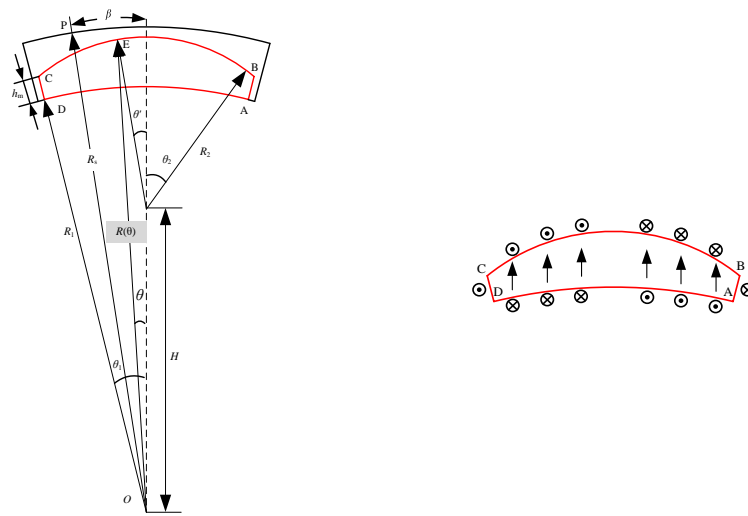


Figure 2. Equivalent surface current.

The density of each surface current can be expressed as:

$$\begin{cases} J_1 = H_c \cos \theta_1 \\ J_2 = H_c \sin \theta' \\ J_3 = H_c \sin \theta \end{cases} \quad (2)$$

where J_1, J_2 , and J_3 represent the surface current density of AB-CD, BC, and AD, respectively; more details of the formula are presented in Appendix C.

$$J_1 = H_c \cos \theta_1 \quad (3)$$

2.2. Calculation of Air-Gap Magnetic Field of a Current-Carrying Coil

The air-gap length is modified by the Carter coefficient, which can be written as Equation (4), without taking into account the cogging effect:

$$c_s = \frac{w_{ss} + w_{st}}{w_{st} + \frac{4g}{\pi} \ln \left(1 + \frac{\pi w_{ss}}{4g} \right)} \quad (4)$$

The length of the equivalent air gap of the structure shown in Figure 3 is:

$$g' = gc_s \quad (5)$$

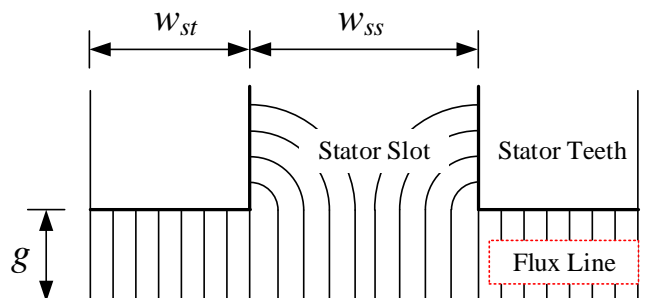


Figure 3. Structure of slot.

The magnetic field produced by a pair of current-carrying coil elements at any point in the air gap is equivalent to two planes with smooth surfaces after the Carter coefficient has been corrected, ignoring the eddy current, hysteresis effects, the saturation effect of the magnetic circuit, and other effects.

The vector magnetic potential generated by a single-turn current-carrying coil at any point P in the air gap shown as Figure 4 can be expressed as:

$$A_z = \begin{cases} \frac{\mu_0 i}{\pi} \sum_{m=1}^{\infty} \frac{R_s^m}{mb^m} \left(\frac{R_r^{2m} + b^{2m}}{R_s^{2m} - R_r^{2m}} \right) \left(\frac{r^m}{R_s^m} + \frac{R_s^m}{r^m} \right) K_{pm} \sin(m\theta) & r \geq b \\ \frac{\mu_0 i}{\pi} \sum_{m=1}^{\infty} \frac{R_s^m}{mb^m} \left(\frac{R_r^{2m} + b^{2m}}{R_s^{2m} - R_r^{2m}} \right) \left(\frac{r^m}{R_r^m} + \frac{R_r^m}{r^m} \right) K_{pm} \sin(m\theta) & r < b \end{cases} \quad (6)$$

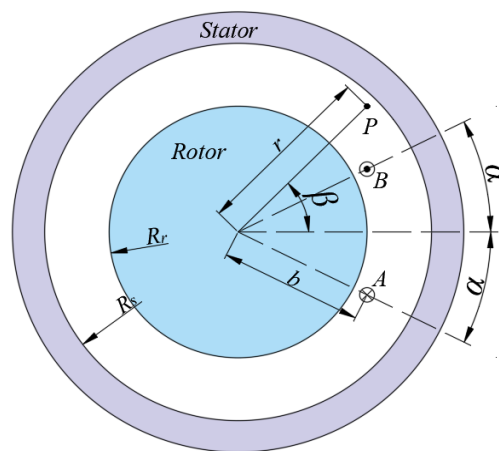


Figure 4. A pair of windings in the air gap.

The SCs are arranged at the slot of the stator, so the magnetic induction intensity can be expressed as:

$$\begin{cases} B_\theta = -\frac{\partial A_z}{\partial r} \\ B_r = \frac{1}{r} \frac{\partial A_z}{\partial \theta} \end{cases} \quad (7)$$

Finally, under the combined action of the three surface currents, the magnetic induction intensity at point P is shown in Equation (8), and the detailed expressions are in Appendix C:

$$\begin{cases} B_r = B_{r1} + B_{r2} + B_{r3} \\ B_t = B_{t1} + B_{t2} + B_{t3} \end{cases} \quad (8)$$

2.3. Calculation of Complex Relative Permeance of Air Gap

The rotor was considered to be equivalent to a smooth surface plane in the previous section’s computation of the air-gap magnetic field. The complex relative permeance is calculated using the complex variable variation method to take into account the stator tooth and slot effect. Since the permanent magnet synchronous motor prototype in this study has a cylindrical rotor core, just the slotting impact of the motor stator needs to be taken into account. The smooth rotor core’s surface is used as a mirror in the mirror method to create the source image and mirror image of each slot in the motor stator, as shown in Figure 5.

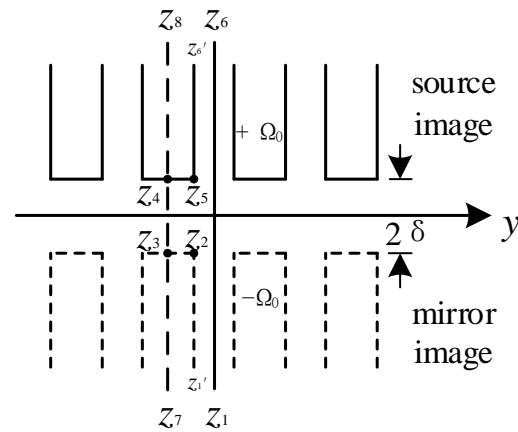


Figure 5. The source image and the mirror image of the stator slot.

Since each slot has the same relative permeance, the relative permeance distribution of the whole motor can be obtained by taking one slot as the calculation unit and repeating it. Since the magnetic field line parallels both the slot center line (Z_1Z_6) and the tooth center line (Z_2Z_8), both of which are magnetic field symmetric lines, the calculation unit for the lowest air gap permeance can be chosen as $Z_1Z_2Z_3Z_4Z_5Z_6$. We assume that the magnetic potential of the mirror surface $Z_1Z_2Z_3$ is $-\Omega_0$ since the scalar magnetic potential of $Z_4Z_5Z_6$ on the stator surface is $+\Omega_0$.

The z -plane is transformed into the upper half-plane of the w -plane and then the t -plane by applying Schwarz–Christoffel (S-C) mapping [38], as shown in Figure 6:

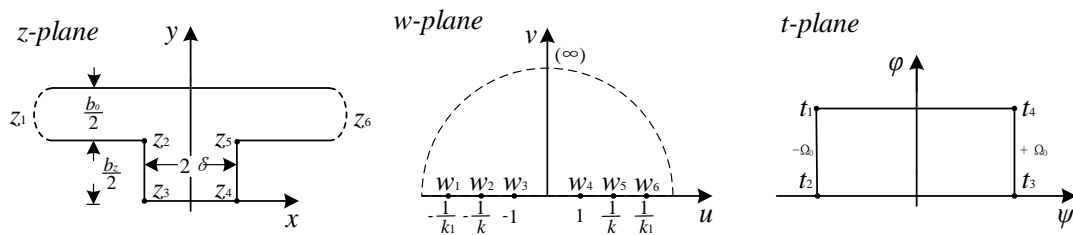


Figure 6. z - w - t plane mapping.

The corresponding mathematical relation in Figure 6 is:

$$\begin{aligned} \frac{dz}{dw} &= S_1 \left(w + \frac{1}{k_1}\right)^{-1} \left(w + \frac{1}{k}\right)^{\frac{1}{2}} (w + 1)^{-\frac{1}{2}} (w - 1)^{-\frac{1}{2}} \left(w - \frac{1}{k}\right)^{\frac{1}{2}} \left(w - \frac{1}{k_1}\right)^{-1} \\ &= S_1' \frac{\sqrt{1-k^2w^2}}{\sqrt{1-w^2}(1-k_1^2w^2)} \end{aligned} \tag{9}$$

$$\frac{dt}{dw} = S_2 \left(w + \frac{1}{k_1}\right)^{-\frac{1}{2}} (w + 1)^{-\frac{1}{2}} (w - 1)^{-\frac{1}{2}} \left(w - \frac{1}{k_1}\right)^{-\frac{1}{2}} \tag{10}$$

After two conformal transformations, the magnetic field distribution in the z plane can be obtained by taking the gradient of the magnetic potential in the t plane:

$$\begin{aligned} B_{slot} &= \mu_0 \frac{dt}{dz} = \mu_0 \frac{dt}{dw} \cdot \frac{dw}{dz} \\ &= \mu_0 \frac{\Omega_0}{K(k_1)} \cdot \frac{1}{\sqrt{1-w^2}\sqrt{1-k_1^2w^2}} \cdot \frac{(1-k_1^2w^2)\sqrt{1-w^2}}{\pi \frac{b_0 \operatorname{sn}(\alpha,k) \cdot \operatorname{dn}(\alpha,k)}{\operatorname{cn}(\alpha,k)} \sqrt{1-k^2w^2}} \\ &= \mu_0 \frac{\pi}{b_0} \cdot \frac{\Omega_0}{K(k_1)} \cdot \frac{\operatorname{cn}(\alpha,k)}{\operatorname{sn}(\alpha,k) \cdot \operatorname{dn}(\alpha,k)} \cdot \frac{\sqrt{1-k_1^2w^2}}{\sqrt{1-k^2w^2}} \end{aligned} \tag{11}$$

When there is no slot, the magnetic density of any point in the z-plane is:

$$B_{\text{slotless}} = \mu_0 \frac{\Omega_0}{\delta} \tag{12}$$

According to Equations (11) and (12), the relative permeance can be calculated:

$$\begin{aligned} \lambda_s &= \frac{B_{\text{slot}}}{B_{\text{slotless}}} \\ &= \mu_0 \frac{\pi}{b_0} \cdot \frac{\Omega_0}{K(k_1)} \cdot \frac{cn(\alpha, k)}{sn(\alpha, k) \cdot dn(\alpha, k)} \cdot \frac{\sqrt{1 - k_1^2 w^2}}{\sqrt{1 - k^2 w^2}} \cdot \frac{1}{\mu_0 \frac{\Omega_0}{\delta}} \\ &= \pi \frac{\delta}{b_0} \cdot \frac{1}{K(k_1)} \cdot \frac{cn(\alpha, k)}{sn(\alpha, k) \cdot dn(\alpha, k)} \cdot \frac{\sqrt{1 - k_1^2 w^2}}{\sqrt{1 - k^2 w^2}} \\ &= \lambda_a + j\lambda_b \end{aligned} \tag{13}$$

w satisfies the following equation:

$$\begin{cases} \frac{b_0}{\pi} \left[u \frac{sn(\alpha, k) \cdot dn(\alpha, k)}{cn(\alpha, k)} - \Pi_j(u, \alpha) \right] - z = 0 \\ w = sn(u, k) \end{cases} \tag{14}$$

where $z = x + jy$ stands for any point in the z plane, and λ_s is a complex number where the real part λ_a and the imaginary part λ_b are the radial and tangential components of the relative permeance, respectively. The induced voltage of the detector coil is:

$$u = \frac{d}{dt} \psi = NS \frac{\sum_{i=1}^m B_i^{t_2} - \sum_{i=1}^m B_i^{t_1}}{t_2 - t_1} \tag{15}$$

where N is the number of turns of the search coil, and S is the area corresponding to the search coil. The magnetic induction intensity of m points is calculated in the space region of each search coil, and B_i^t is the value of magnetic induction at time t at position i in space.

2.4. Search Coil Arrangement Scheme

The search coils sense the information about the magnetic field in the air gap and reflect the motor condition. In order to prevent the search coils from any damage during the wiring process of the motor winding, they are usually arranged at the slot after it is wired down. In order to make the magnetic fields compensate for each other in a healthy state, two detection coils are arranged one pole apart and reversed in series, as shown in Figures 7 and 8.

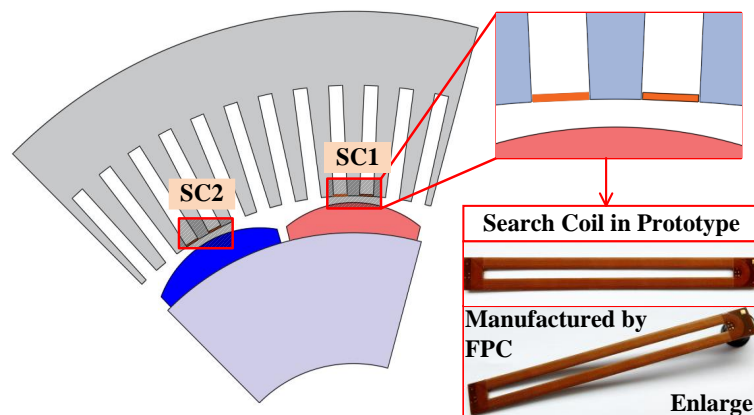


Figure 7. Search coil arrangement scheme.

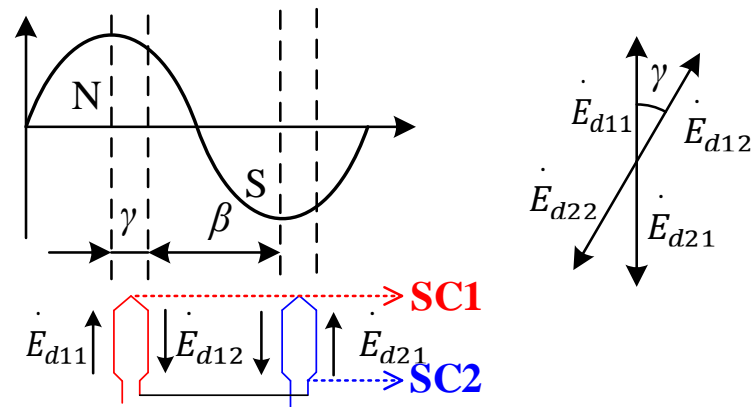


Figure 8. The two coils are connected in series in reverse.

3. Results

The proposed fault detection method is first validated by simulation. The main parameters of the studied PMSM are listed in Table 1.

Table 1. Main Parameters of PMSM.

Parameter	Value	Parameter	Value
Rated Power (kW)	0.94	Rated Speed (r/min)	300
Rated Torque (Nm)	30	Stator Resistance (Ω)	4.3
Number of Pole Pairs	6	PM Flux Linkage (wb)	0.98

The induced voltage signal obtained from the search coil needs to be further processed to achieve the fault detection strategy proposed in this paper. The specific process is shown in Figure 9. Velocity normalization and angle domain transformation are the core of this paper. On the one hand, this can ensure the applicability of the detection scheme under dynamic operation, and on the other hand, this also lays a foundation for the quantitative description of subsequent fault degree. It can be seen that the data processing flow of EMF is similar to the experiment; the difference is that the problem of interference by non-ideal factors in the experimental process needs additional processing.

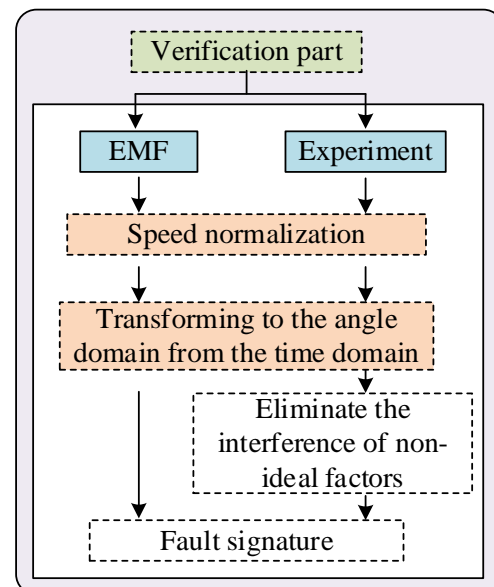


Figure 9. Signal processing flow.

3.1. Simulation Results

Firstly, it is established that theoretical calculations and simulation calculations are consistent; the results are shown in Figure 10. Indicating the correctness of the theoretical calculation, the calculated value of magnetic induction intensity and the induced voltage in the search coil are in close agreement.

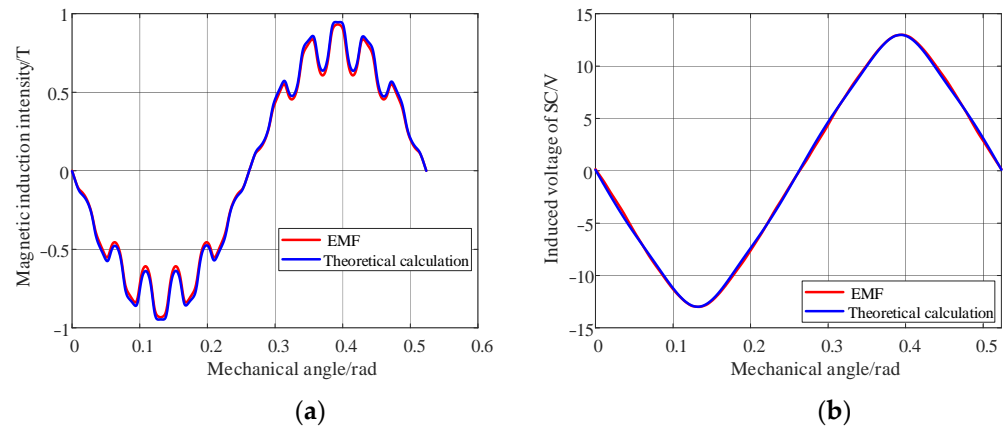


Figure 10. Comparison of theoretical calculation and simulation results. (a) Magnetic induction intensity calculation results. (b) The calculation result of the induced voltage in the search coil.

There are two types of simulation content. The first, which corresponds to the theoretical analysis above, simulates demagnetization failure by altering the permanent magnet's remanence, which is the same as the demagnetization itself. In this article, a new modeling scheme was implemented to simulate the demagnetization fault more simply. A concentric coil with specific numbers of turns was wound on the surface of the permanent magnet, and the current was then injected into the coil. The permanent magnet's magnetic field was counteracted by the injected current in the opposite direction, and the demagnetization defect was mimicked.

(a) Changing the remanence of the permanent magnet

The demagnetization process of the permanent magnet is shown in Figure 11. Irreversible demagnetization occurs when the working point crosses the knee point *K* and reaches the point *Q*, and then returns along the route indicated by the red dotted line. Compared with the healthy state, the remanence value after demagnetization will be significantly reduced. As a result, by altering the remanence of the permanent magnet material in the finite element model, the demagnetization fault can be recreated.

The remanence value of the faulty permanent magnet is set to 0.9 times, 0.8 times, and 0.7 times the normal state to simulate 10%, 20%, and 30% demagnetization failures, respectively. The magnetic field determined by theoretical calculation and simulation is shown in Figure 12a; the red curve represents the space air gap magnetic field in a healthy state, while the blue curve represents the fault state. The space magnetic field intensity corresponding to the faulty magnet decreases significantly. Figure 12b shows how the induced voltage in the two detection coils changes with the position of the rotor. Since the detection coil is fixed on the stator teeth, when the faulty permanent magnet rotates through the detection coil, the amplitude of the induced voltage in the detection coil decreases significantly, as shown in Figure 12c for local amplification.

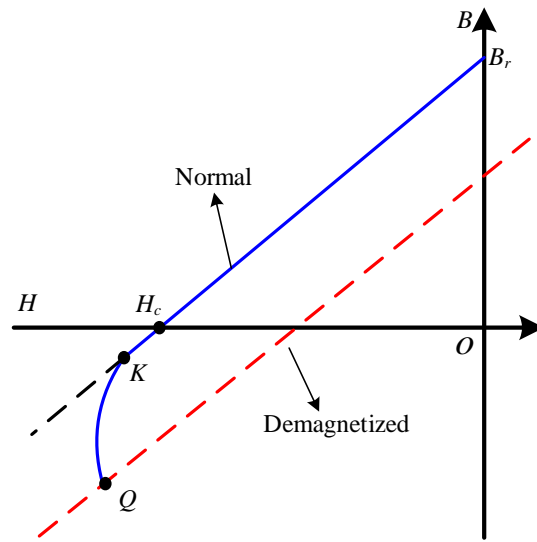


Figure 11. The demagnetization curve of permanent magnetic material.

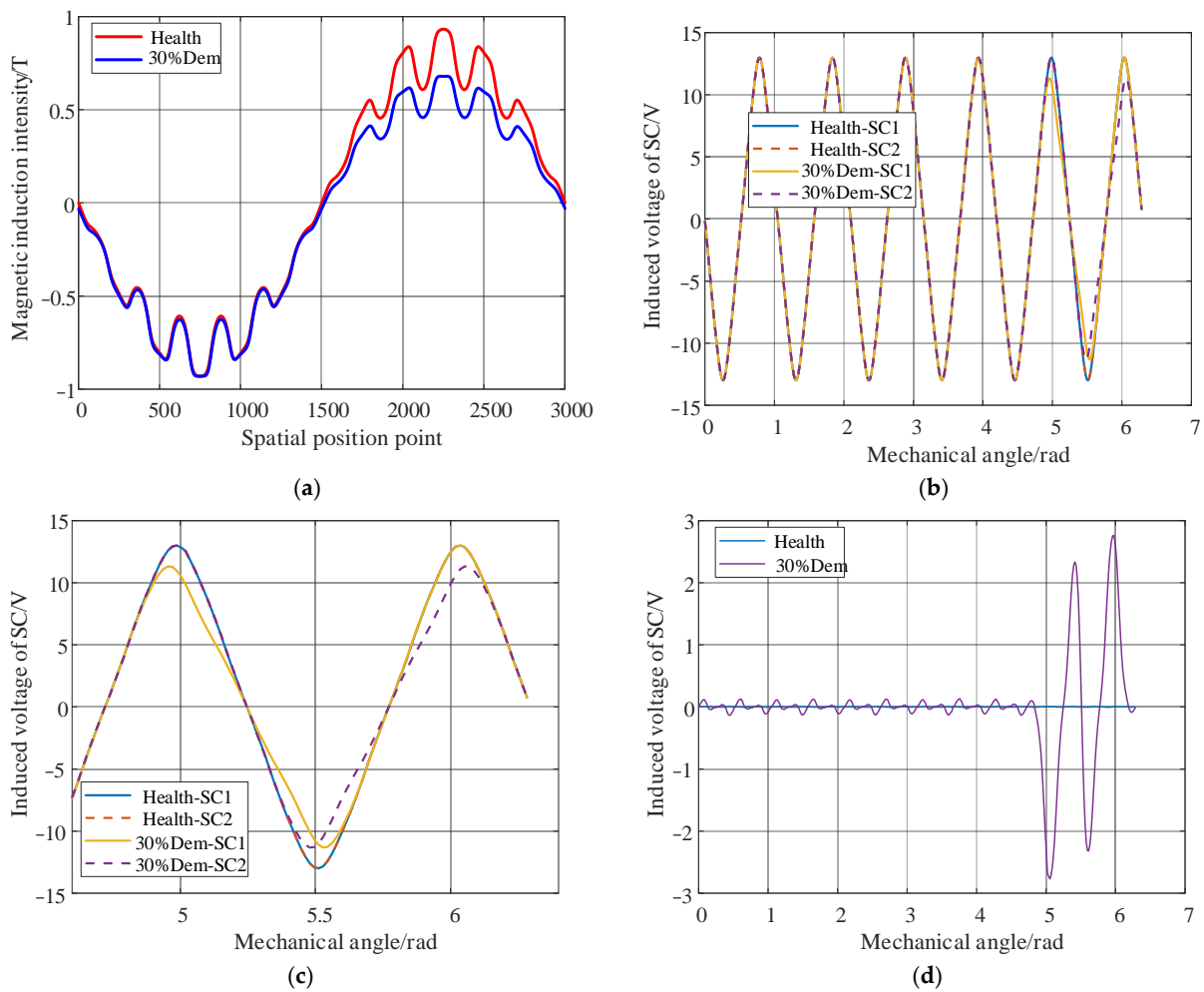


Figure 12. Simulation results of demagnetization failure. (a) Results for the air-gap magnetic field during 30% demagnetization. (b) Output voltage of two search coils under healthy condition and 30% demagnetization. (c) Local magnification of induced voltage of search coil. (d) The output of the search coil in series under healthy condition and 30% demagnetization.

Accordingly, regardless of the fault or health status, the shape of the output voltage waveform of the two detection coils is the same, but there is a fixed phase difference, as illustrated in Figure 12b,c. As can be seen, the two search coils are positioned 30 degrees apart in space. Due to the existence of this phase difference, the output voltage of the two search coils cannot be eliminated in the faulty state depicted in Figure 12d, making the demagnetization fault detectable.

The output of two search coils connected in series under various degrees of demagnetization failure is displayed in Figure 13a. Suppose the flux linkage in Equation (15) is expressed as follows:

$$\psi = \varphi \cos(\omega t) \tag{16}$$

where φ is the flux amplitude. From Equations (15) and (16):

$$\begin{aligned} u &= \frac{d}{dt}[\varphi \cos(\omega t)] = -\omega\varphi \sin(\omega t) \\ &= -\omega\varphi \sin(\theta) \end{aligned} \tag{17}$$

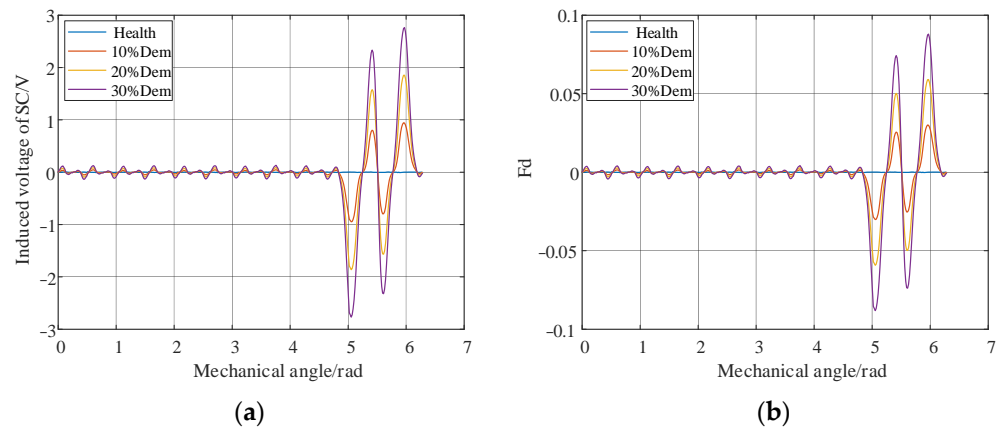


Figure 13. Simulation results of demagnetization failure. (a) The output result of the search coil in series under different degrees of demagnetization failure. (b) Fd value under different fault degrees.

It follows that the output voltage and speed are inversely proportional. The permanent magnet motor’s rotor position may be easily collected from the system because it is a crucial parameter in the control process. Fault-related parameters regarding rotor position angle are defined as follows:

$$Fd = \frac{u}{\omega} = -\varphi \sin(\theta) \tag{18}$$

The output voltage difference and Fd value under different fault degrees are shown in Figure 13.

Figure 13 shows that when a single permanent magnet is demagnetized, the spatial magnetic field is primarily distorted near the magnet. This allows the entire circle to be divided into set angles, with each piece representing a pole. The area between each piece and the x-axis is then determined, and this area is referred to as the periodic energy value in this context. Figure 14 depicts the simulation result at a 10% degree of demagnetization. The output signal is not zero, and the matching periodic energy value is not zero when the fault magnet is rotated close to the search coil.

Figure 15 displays the simulation results for various fault degrees. The link between the two is roughly linear, and as the fault degree grows, so does the related energy value.

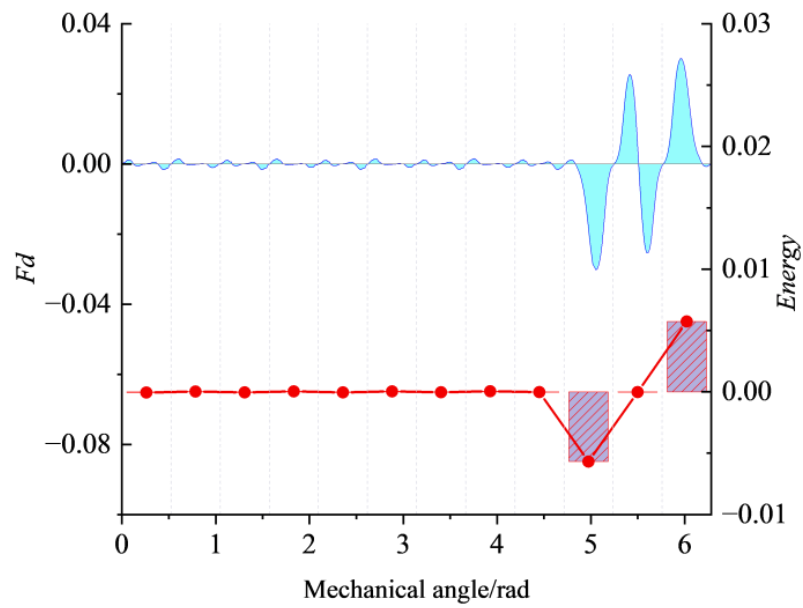


Figure 14. The periodic energy value when the demagnetization degree is 10% where the blue line represents F_d and red represents $Energy$.

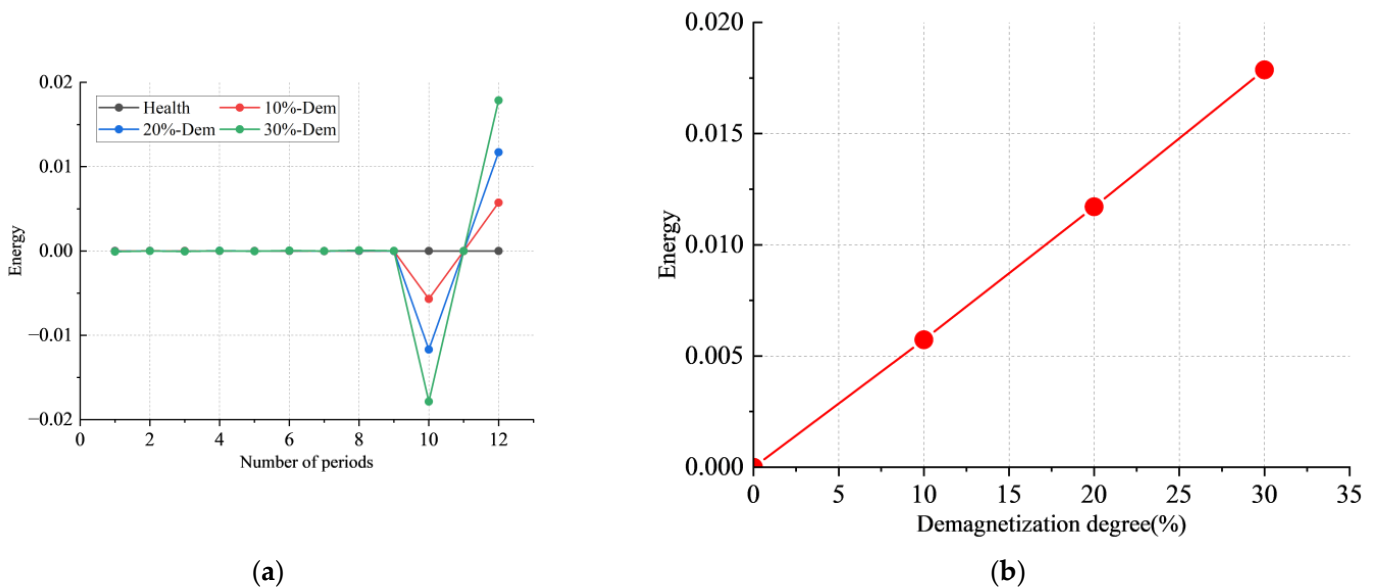


Figure 15. Simulation results under different fault degrees. (a) The periodic energy value under different fault degrees. (b) Relationship between maximum energy value and demagnetization ratio.

(b) Applying demagnetizing excitation

The traditional method for simulating demagnetization fault removes a part of the permanent magnet, even if it is closer to the actual fault. This method has some other drawbacks, such as difficulty in disassembling and the inability to set different fault degrees. Therefore, a concentric coil is wound on the surface of the permanent magnet, and then a magnetic field opposite to the direction of the permanent magnet is generated by passing a current into the coil, as shown in Figure 16.

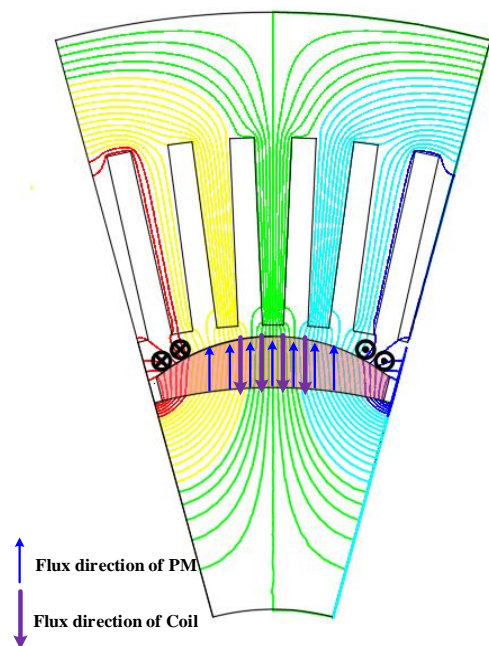


Figure 16. Working principle of demagnetizing coil.

In order to avoid any excessive demagnetization current leading to irreversible demagnetization of the permanent magnet and considering the maximum carrying capacity of the current source, 5 A, 10 A, and 15 A currents are passed into the demagnetization coil in three scenarios.

The difference in periodic energy values between Figures 15 and 17 is roughly an order of magnitude. It is assumed that the degree of demagnetization simulated by the injection demagnetization current is very small. To further demonstrate this hypothesis, the amplitude variation of the fundamental frequency component of the induced voltage in the search coil is utilized as the reference for the simulation analysis to match the injection current in the demagnetization coil to the degree of demagnetization of the permanent magnet.

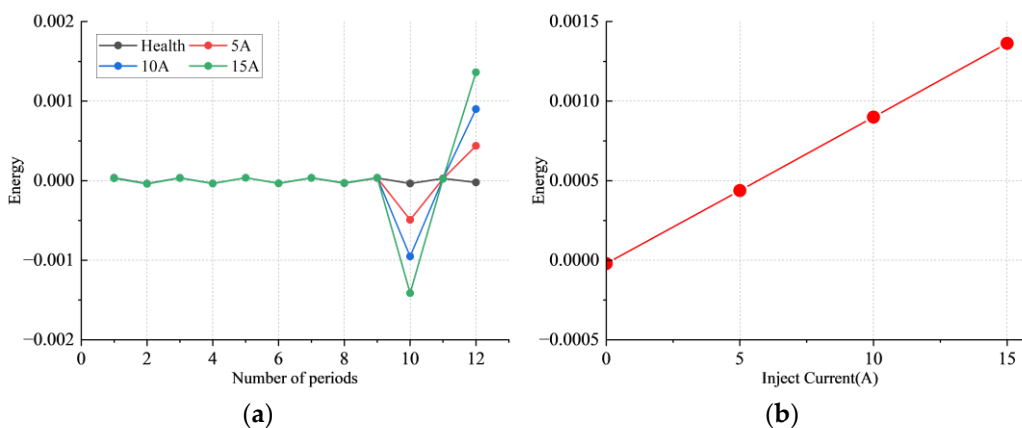


Figure 17. Simulation results under different injecting currents. (a) Periodic energy value under different fault degrees. (b) Relationship between maximum energy value and injecting current.

The simulation results are shown in Figure 18. The first intersection point in the upper left corner is taken as an example. When the amplitude of the induced voltage of the probe coil is 11.568 V, it is found that the corresponding injection current of the demagnetization coil is 15 A, and the demagnetization ratio of the permanent magnet is 3.35157%. The primary cause is that the injected current value is not large enough, and the number of

turns of the demagnetization coil is also relatively small due to the limited spatial position. So, the degree of the simulated fault is relatively small. However, the two curves have the same trend, which depicts the reliability of the simulation.

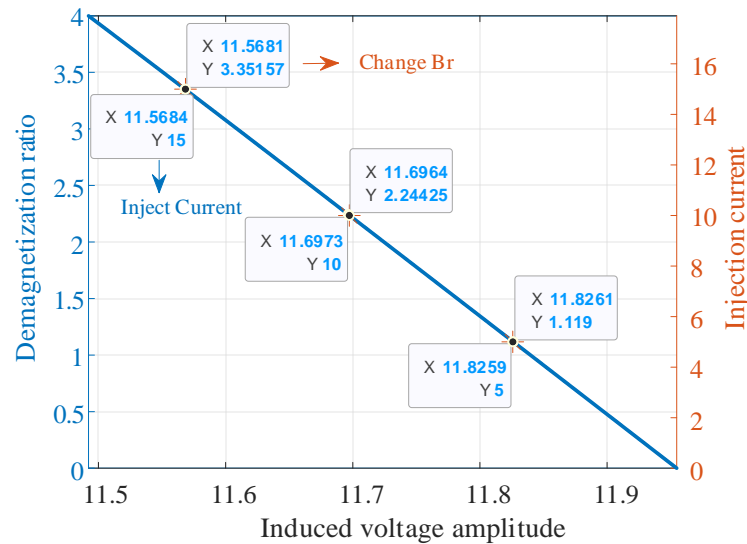


Figure 18. Relationship between injection current and demagnetization ratio.

3.2. Experimental Platform

A laboratory-based experimental platform was constructed, as depicted in Figure 19, to confirm the efficacy of the suggested strategy. A PMSM, a DC power supply used to inject current into the demagnetizing coil (DM coil), an induction motor serving as the load, and a six-phase inverter with a 2 kHz switching frequency make up the experimental platform. The experimental data were collected using a recorder at a 500 kHz sampling rate.

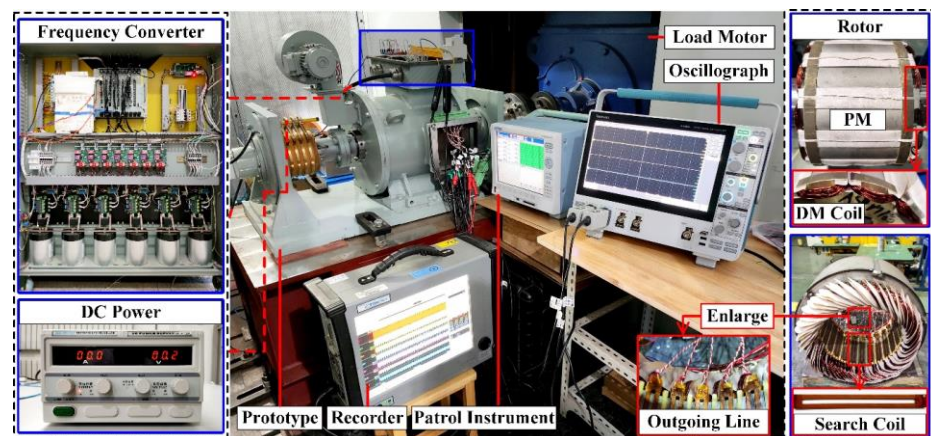


Figure 19. Experimental platform.

High-strength fibers are wound to secure the demagnetization coil, which is wound on the permanent magnet’s surface. The carbon brush slip ring structure connects the demagnetization coil, which is situated at the rotor, to the external power source.

3.3. Experimental Results

Induced voltage is the initial signal collected from the search coil; the time-domain waveform and local amplification are displayed in Figure 20.

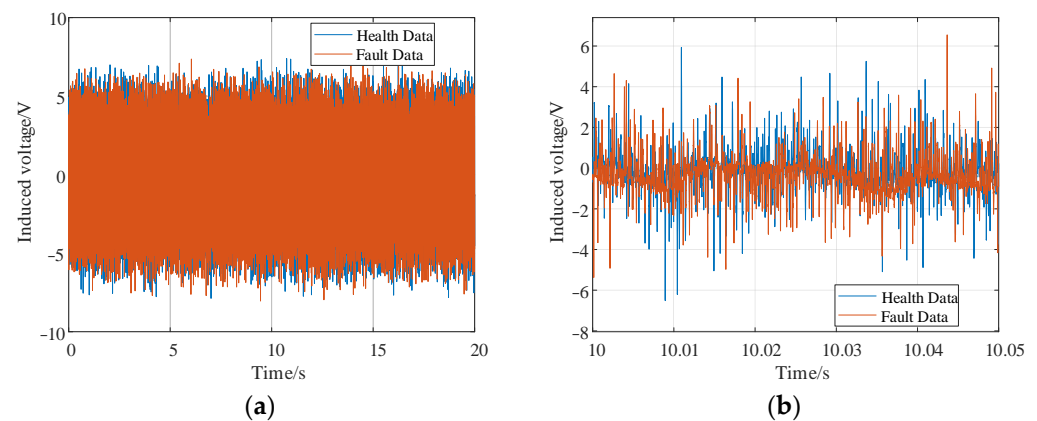


Figure 20. Time-domain waveform of the search coil. (a) Whole-time domain data. (b) Partially enlarged detail.

The time-domain waveform of the induced voltage is highly complicated due to the abundant magnetic field information because the search coil is positioned in the air gap of the motor, and the fault information brought by demagnetization is then buried. On the other hand, because of the presence of non-ideal elements, such as the search coil's incorrect placement and the permanent magnet's innate dispersion, the signal in the search coil cannot be eliminated, even when the motor is in good health. As a result, this study opts to directly subtract the health status data from the fault data, and the resulting difference will include the fault information. The motor operation process, however, cannot be operated directly in the time domain because it is an unstable process; as a result, the signals must undergo the following processing:

Following Equation (18), the original signal is divided by the angular velocity to produce the characteristic quantity Fd that is speed independent. It is important to note that the rotor position angle is a crucial component of the permanent magnet synchronous motor's operation control, so the speed normalization operation, in this case, can acquire the speed information directly from the control system without the need for extra devices.

As can be observed from Equation (18), the value of Fd only has a relationship with the flux amplitude and angle sine function; hence, for the same angle, the value will accurately reflect the motor's state of health. The relationship between the output value of the search coil and the electrical angle under the healthy and fault states is derived by processing the aforementioned two processes, as shown in Figure 21a. The blue curve represents the fault characteristic value under the condition of health, which is always zero under ideal circumstances—but it is not zero due to the existence of non-ideal factors such as the installation error of the search coil—while the red curve represents the characteristic value under the fault state. Compared with the blue curve, when the fault permanent magnet rotates through the search coil, the characteristic value changes significantly. The difference between the health and failure states is shown in Figure 21b. It goes without saying that when a single permanent magnet fails and rotates close to the search coil, the characteristic parameter Fd obviously increases.

The same processing approach as in Figure 14 is used here. The characteristic parameter Fd is integrated according to a predetermined electrical angle to yield the findings displayed in Figure 22 that quantitatively reflect the fault degree.

According to the simulation results, the energy value at this location changes noticeably as the fault magnet passes through the search coil, whereas the energy value at other locations is very close to zero.

(a) Changing the demagnetizing current

As depicted in Figure 19, a DC power source is used to inject currents into the demagnetizing coil that are varied in value while maintaining the speed and load, and the test results are displayed in Figure 23.

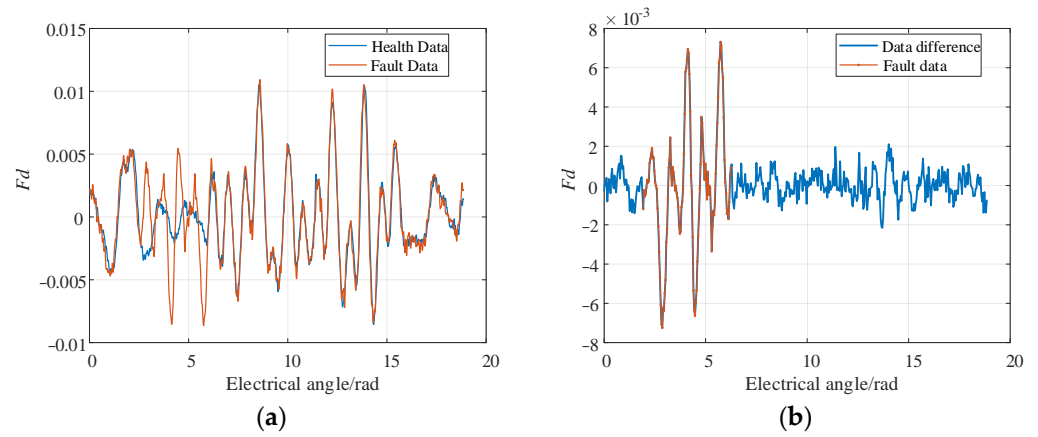


Figure 21. The output waveform of the search coil in one mechanical cycle under both health and failure conditions. (a) Initial waveforms in fault and health states. (b) Fault and health difference waveform where the red line is the faulty magnet rotating through the search coil.

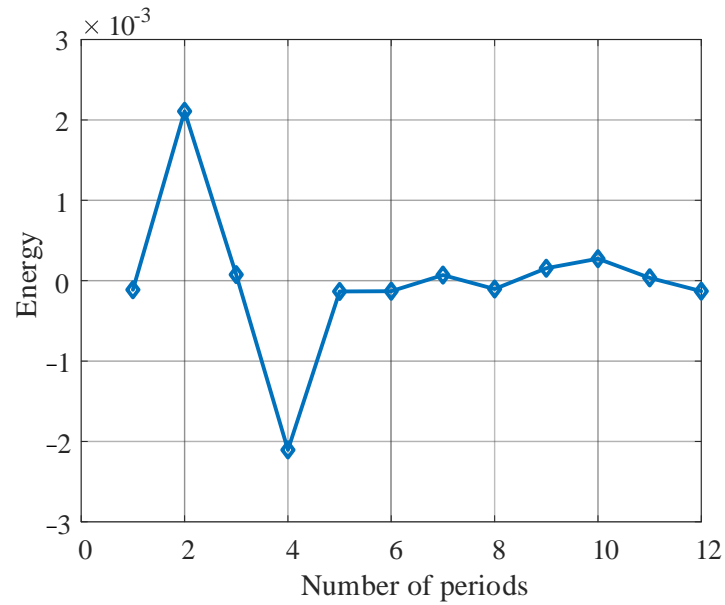


Figure 22. The periodic energy value when the injection current is 15 A.

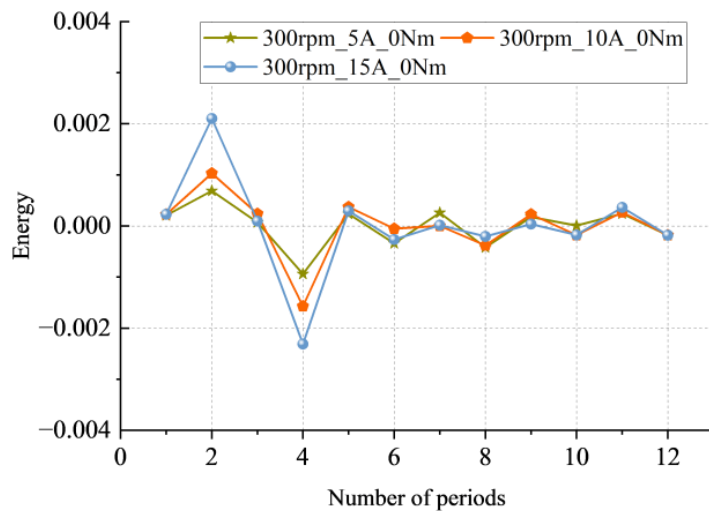


Figure 23. Test results of different demagnetizing currents under 300 rpm and 0 Nm.

Consistent with the simulation results, the periodic energy value of the location of the fault increases with the increase in the injected demagnetization current. A difference can be seen even with the injection of 5 A demagnetization current, equivalent to a 1.1% demagnetization ratio.

(b) Change in load

The aforementioned theoretical study is predicated on the stator’s total symmetry; thus, there won’t be any impact on the detection of demagnetization faults because there won’t be any different signals in the detection coil under various loads. Test verification was carried out, and the results are shown in Figure 24:

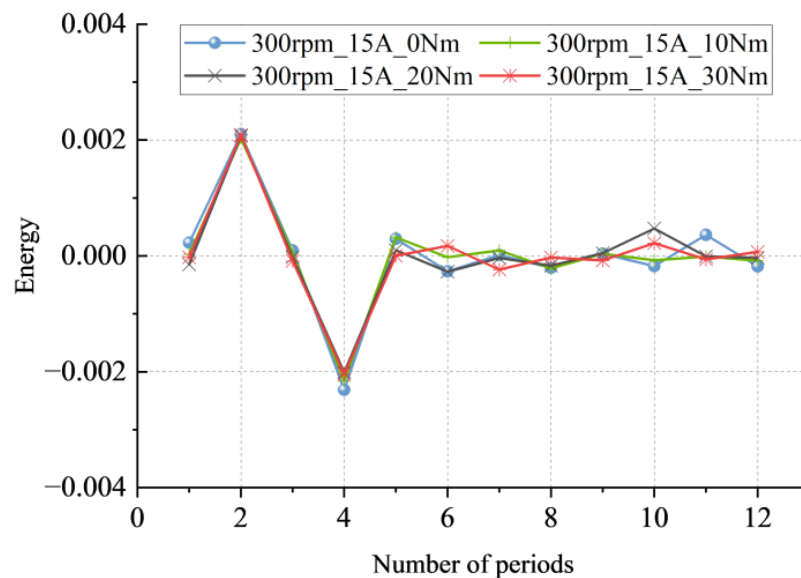


Figure 24. Test results under different loads when the rotating speed is 300 rpm, and the injection demagnetization current is 15 A.

These findings demonstrate that the detection outcomes are essentially consistent under various loads, demonstrating the proposed scheme’s load immunity.

(c) Change in speed

Figure 25 displays the test results at various running speeds with the same load and a similar-sized demagnetizing current.

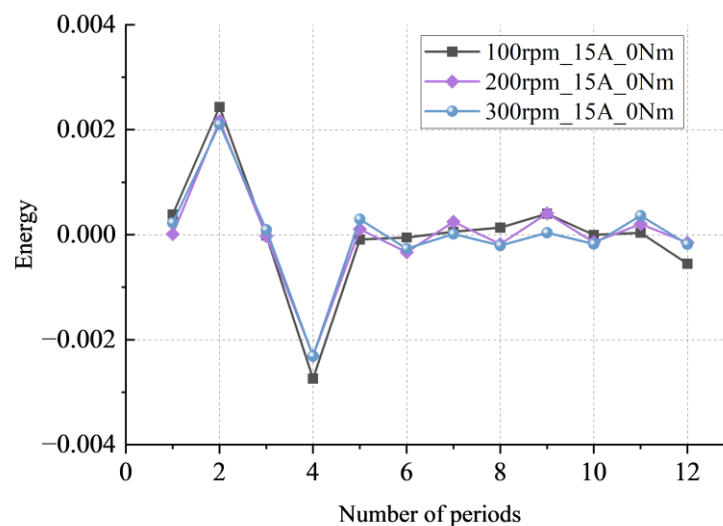


Figure 25. Test results at different rotational speeds.

The detection results under various speeds can be found to be essentially consistent, demonstrating the robustness of the detection technique to the speed.

Experimental results under variable speed operation are shown in Figure 26.

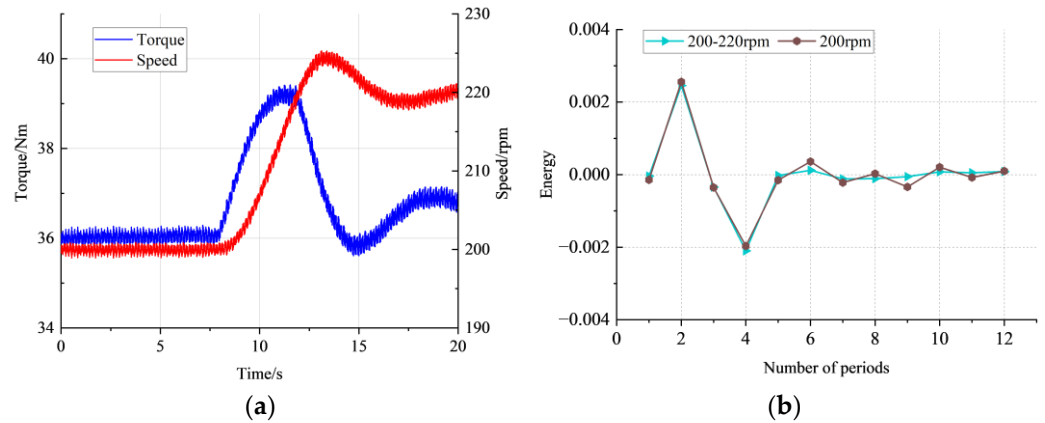


Figure 26. Test results under different dynamic conditions. (a) Speed and torque dynamic curve. (b) Demagnetization test results.

It can be seen from Figure 26a that torque changes are also included in the process of the motor running from one steady-state speed to another. The experimental results for dynamic operation are consistent with those for steady-state operation from Figure 26b, showing that the method proposed in this paper is not affected by the operating condition of the motor and still has a good detection effect under dynamic operation.

4. Discussion

Table 2 summarizes the main properties of existing techniques for the particular case of PM demagnetization detection. Motor current signature analysis (MCSA) relies on observing specific harmonics in the stator current spectrum for fault detection. It should be noted that the rotor dynamic eccentricity will also produce the same frequency component. Although the method of high-frequency signal injection (HFI) can distinguish between demagnetization and eccentricity, the detection effect is highly dependent on the motor parameters. Hall-effect sensors are typically used to measure leakage flux, but a suitable installation location needs to be reserved for the design of the motor before it is manufactured. SC-based methods overcome most of these limitations. It is important to note that none of the existing studies on demagnetization fault diagnosis using SCs can be applied to dynamic operation, which is the value of this paper.

Table 2. Comparative analysis of fault detection techniques.

	MCSA [12,14,24]	Hall-Effect [39–41]	HFI [15,34]	SCs [4,36,42,43]	Proposed Method
Low cost	✓	✓	✓	✓	✓
Non-invasive	✓	x	✓	x	x
Dynamic property	✓	✓	x	x	✓
Independent of parameters	✓	✓	x	✓	✓
Low computational burden	x	✓	x	✓	✓

Compared with MCSA and HFI, the invasiveness of the proposed method is its inherent defect. However, once it is installed in the motor, additional maintenance does not need to be carried out, and only two search coils are required to achieve demagnetization fault detection, which is great progress compared to the existing search coil scheme. It is important that the proposed scheme solves the problem of demagnetization fault detection under the dynamic operation of the motor without a complicated calculation method, which greatly improves the rapid response ability of demagnetization fault detection. On the other hand, the experimental results verify that the proposed scheme can achieve 1.1% demagnetization fault detection, which represents a very high detection sensitivity.

5. Conclusions

This paper focuses on the local demagnetization fault of PMSMs and presents a period energy-based method for diagnosing demagnetization faults in permanent magnet motors without taking into account the operating conditions of the motor by transforming the flux information in the time domain into the angle domain and normalizing speed. At the same time, to eliminate the influence of the installation error of the search coil and the dispersion of the permanent magnet itself on the detection results, the paper takes a set of magnetic flux data without demagnetization as the reference and subtracts the measured magnetic flux data with the reference data mentioned above to obtain the characteristic data reflecting the fault information. The experimental results show that the demagnetization ratio of 1.1% can be achieved. For motor fault monitoring in unsteady state operations, such as electric automobiles, this technique has significant ramifications. For the local demagnetization fault, the signal distortion in the search coil will only be caused when the faulty permanent magnet rotates near the search coil. Therefore, the whole circle is segmented according to the angle corresponding to the permanent magnet sweeping through the search coil, and the periodic energy value is defined as the fault indicator. When the motor is functioning normally, this indicator value is close to zero; nevertheless, if a failure occurs, it will be much more than zero. It is essential that this fault detection indication simply relates to the severity of the defect and is unrelated to the motor's running condition. However, more research is required to fully understand the mapping between the degree of fault and eigenvalues. Simultaneous demagnetization of multiple permanent magnets and the demagnetization fault detection of the motor at a standstill are critical problems to be overcome.

Author Contributions: Conceptualization, W.H. and J.H.; methodology, W.H., W.S. and J.H.; software, W.H. and H.L.; validation, W.H. and K.L.; formal analysis, W.H.; writing—original draft preparation, W.H.; writing—review and editing, W.H., J.H. and J.C. All authors have read and agreed to the published version of the manuscript.

Funding: This research was funded by the National Natural Science Foundation of China, grant numbers 51825703 and 52207047.

Data Availability Statement: Not applicable.

Acknowledgments: The authors would like to thank for the funding from the National Natural Science Foundation of China.

Conflicts of Interest: The authors declare no conflict of interest.

Appendix A

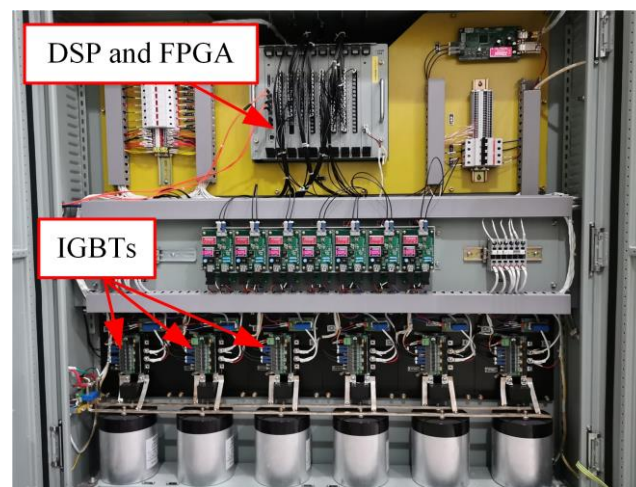
The detailed dimensions and materials of the motor are shown in Table A1.

Table A1. The main dimensions and materials of the six-phase surface PMSM.

Parameter	Value	Parameter	Value
Length of the unilateral air gap	2 mm	Slot width	4.2 mm
Stator outer diameter	290 mm	Thickness of permanent magnet	9 mm
Inner diameter of the stator	180 mm	Overlaying coefficient	0.97
Rotor outer diameter	176 mm	Number of stator slots	72
Inside diameter of the rotor	80 mm	Number of conductors per slot	72
Stator core length	88 mm	Number of parallel branches	1
Yoke thickness	22 mm	Pitch	6
Stator core material	50WW310	Winding coefficient	1
Rotor core material	16 Mn	Permanent magnet material	SmCo30

Appendix B

Based on a six-phase surface-mount permanent magnet synchronous motor system, the demagnetization fault is studied in this paper. The inverter is shown in Figure A1. The Insulated Gate Bipolar Transistor (IGBT) module is PM75RLA120 from Mitsubishi, the field programmable gate array (FPGA) chip is XC4VLX25-11FFG668I from XILINX, the digital signal processing (DSP) chip is TMS320F28335 from Texas Instruments, the current sensor is 55-P/SP50 from LEM Company LA, and the decoding chip is ADS1203 from Texas Instruments company.

**Figure A1.** Six-phase H-bridge inverter.

Appendix C

The current micro-element along the AB and CD sides is:

$$di_1 = H_c \cos \theta_1 dr \quad (\text{A1})$$

The infinitesimal equivalent surface current on the BC side is:

$$di_2 = H_c \sin \theta' R_2 d\theta' \quad (\text{A2})$$

θ and θ' are the central angles corresponding to any point on the inner and outer surfaces of the permanent magnet, respectively. From the geometric relationship in Figure 2, it can be deduced:

$$\theta' = \arcsin\left(\frac{H}{R_2} \sin \theta\right) + \theta \quad (\text{A3})$$

$$R(\theta) = \frac{R_2}{\sin \theta} \sin \theta' \tag{A4}$$

$$d\theta' = \left(1 + \frac{H \cos \theta}{\sqrt{R_2^2 - H^2 \sin^2 \theta}} \right) d\theta \tag{A5}$$

The equivalent surface current of the AD side is:

$$di_3 = H_c \sin \theta R_1 d\theta \tag{A6}$$

$$B_r = \frac{\mu_0 i}{\pi r} \sum_1^\infty \frac{R_s^m}{a^m} \left(\frac{R_1^{2m} + a^{2m}}{R_s^{2m} - R_1^{2m}} \right) \left(\frac{r^m}{R_s^m} + \frac{R_s^m}{r^m} \right) k_{pm} \cos m\beta \tag{A7}$$

$$B_\theta = -\frac{\mu_0 i}{\pi r} \sum_1^\infty \frac{R_s^m}{a^m} \left(\frac{R_1^{2m} + a^{2m}}{R_s^{2m} - R_1^{2m}} \right) \left(\frac{r^m}{R_s^m} - \frac{R_s^m}{r^m} \right) k_{pm} \sin m\beta \tag{A8}$$

The magnetic induction intensity generated by the AB-CD surface current at point *P* is:

$$\begin{aligned} B_{r1} &= \int_{R_1}^{R_1+h_m} \left[\frac{\mu_0 H_c \cos \theta_1}{\pi r} \sum_1^\infty \frac{R_s^m}{a^m} \left(\frac{R_1^{2m} + a^{2m}}{R_s^{2m} - R_1^{2m}} \right) \left(\frac{r^m}{R_s^m} + \frac{R_s^m}{r^m} \right) k_{pm} \cos m\theta \right] da \\ &= \frac{\mu_0 H_c R_s^m \cos \theta_1}{\pi r} \left(\frac{r^m}{R_s^m} + \frac{R_s^m}{r^m} \right) k_{pm} \cos m\theta \int_{R_1}^{R_1+h_m} \left[\sum_1^\infty \frac{1}{a^m} \left(\frac{R_1^{2m} + a^{2m}}{R_s^{2m} - R_1^{2m}} \right) \right] da \end{aligned} \tag{A9}$$

$$\begin{aligned} B_{\theta1} &= \int_{R_1}^{R_1+h_m} \left[-\frac{\mu_0 H_c \cos \theta_1}{\pi r} \sum_1^\infty \frac{R_s^m}{a^m} \left(\frac{R_1^{2m} + a^{2m}}{R_s^{2m} - R_1^{2m}} \right) \left(\frac{r^m}{R_s^m} - \frac{R_s^m}{r^m} \right) k_{pm} \sin m\theta \right] da \\ &= -\frac{\mu_0 H_c R_s^m \cos \theta_1}{\pi r} \left(\frac{r^m}{R_s^m} - \frac{R_s^m}{r^m} \right) k_{pm} \sin m\theta \int_{R_1}^{R_1+h_m} \left[\sum_1^\infty \frac{1}{a^m} \left(\frac{R_1^{2m} + a^{2m}}{R_s^{2m} - R_1^{2m}} \right) \right] da \end{aligned} \tag{A10}$$

Similarly, the magnetic induction intensity generated by the AD surface current at point *P* is:

$$B_{r3} = \frac{\mu_0 H_c R_1 R_s^m}{\pi r} \cdot \left(\frac{r^m}{R_s^m} + \frac{R_s^m}{r^m} \right) \cdot k_{pm} \cos m\beta \cdot \sum_1^\infty \frac{1}{a^m} \left(\frac{R_1^{2m} + a^{2m}}{R_s^{2m} - R_1^{2m}} \right) \cdot (1 - \cos \theta_1) \tag{A11}$$

$$B_{t3} = \frac{\mu_0 H_c R_1 R_s^m}{\pi r} \cdot \left(\frac{r^m}{R_s^m} - \frac{R_s^m}{r^m} \right) \cdot k_{pm} \sin m\beta \cdot \sum_1^\infty \frac{1}{a^m} \left(\frac{R_1^{2m} + a^{2m}}{R_s^{2m} - R_1^{2m}} \right) \cdot (\cos \theta_1 - 1) \tag{A12}$$

Only its differential expression is provided here because there is no explicit expression for the magnetic induction strength generated by the BC planar current at point *P*:

$$\left\{ \begin{aligned} B_{r2} &= \int_0^{\theta_1} \frac{\mu_0 H_c \sin \theta' R_2}{\pi r} \sum_1^\infty \frac{R_s^m}{a^m} \left(\frac{R_1^{2m} + a^{2m}}{R_s^{2m} - R_1^{2m}} \right) \left(\frac{r^m}{R_s^m} + \frac{R_s^m}{r^m} \right) k_{pm} \cos m\beta \left(1 + \frac{H \cos \theta}{\sqrt{R_2^2 - H^2 \sin^2 \theta}} \right) d\theta \\ &\quad a = R(\theta) = \frac{R_2}{\sin \theta} \sin \theta' \\ &\quad \theta' = \arcsin \left(\frac{H}{R_2} \sin \theta \right) + \theta \end{aligned} \right. \tag{A13}$$

$$\left\{ \begin{aligned} B_{t2} &= -\int_0^{\theta_1} \frac{\mu_0 H_c \sin \theta' R_2 R_s^m}{\pi r} \cdot \left(\frac{r^m}{R_s^m} - \frac{R_s^m}{r^m} \right) \cdot k_{pm} \sin m\beta \cdot \sum_1^\infty \frac{1}{a^m} \left(\frac{R_1^{2m} + a^{2m}}{R_s^{2m} - R_1^{2m}} \right) \left(1 + \frac{H \cos \theta}{\sqrt{R_2^2 - H^2 \sin^2 \theta}} \right) d\theta \\ &\quad a = R(\theta) = \frac{R_2}{\sin \theta} \sin \theta' \\ &\quad \theta' = \arcsin \left(\frac{H}{R_2} \sin \theta \right) + \theta \end{aligned} \right. \tag{A14}$$

References

1. Zdorovets, M.V.; Kozlovskiy, A.L.; Shlimas, D.I.; Borgekov, D.B. Phase transformations in FeCo—Fe₂CoO₄/Co₃O₄-spinel nanostructures as a result of thermal annealing and their practical application. *J. Mater. Sci. Mater. Electron.* **2021**, *32*, 16694–16705. [[CrossRef](#)]
2. Turchenko, V.A.; Trukhanov, S.V.; Balagurov, A.M.; Kostishyn, V.G.; Trukhanov, A.V.; Panina, L.V.; Trukhanova, E.L. Features of crystal structure and dual ferroic properties of BaFe_{12-x}Me_xO₁₉ (Me = In³⁺ and Ga³⁺; x = 0.1–1.2). *J. Magn. Magn. Mater.* **2018**, *464*, 139–147. [[CrossRef](#)]
3. Huang, F.; Zhang, X.; Qin, G.; Xie, J.; Peng, J.; Huang, S.; Long, Z.; Tang, Y. Demagnetization Fault Diagnosis of Permanent Magnet Synchronous Motors Using Magnetic Leakage Signals. *IEEE Trans. Ind. Inform.* **2023**, *19*, 6105–6116. [[CrossRef](#)]
4. Rafaq, M.S.; Lee, H.J.; Park, Y.; Lee, S.B.; Zapico, M.O.; Fernandez, D.; Reigosa, D.; Briz, F. Airgap Search Coil Based Identification of PM Synchronous Motor Defects. *IEEE Trans. Ind. Electron.* **2022**, *69*, 6551–6560. [[CrossRef](#)]
5. Faiz, J.; Mazaheri-Tehrani, E. Demagnetization Modeling and Fault Diagnosing Techniques in Permanent Magnet Machines Under Stationary and Nonstationary Conditions: An Overview. *IEEE Trans. Ind. Appl.* **2017**, *53*, 2772–2785. [[CrossRef](#)]
6. Zhivulin, V.E.; Trofimov, E.A.; Zaitseva, O.V.; Sherstyuk, D.P.; Cherkasova, N.A.; Taskaev, S.V.; Vinnik, D.A.; Alekhina, Y.A.; Perov, N.S.; Naidu, K.C.B.; et al. Preparation, phase stability, and magnetization behavior of high entropy hexaferrites. *iScience* **2023**, *26*, 107077. [[CrossRef](#)]
7. Tuleushev, A.Z.; Harrison, F.E.; Kozlovskiy, A.L.; Zdorovets, M.V. Evolution of the absorption edge of PET films irradiated with Kr ions after thermal annealing and ageing. *Opt. Mater.* **2021**, *119*, 111348. [[CrossRef](#)]
8. Kozlovskiy, A.L.; Shlimas, D.I.; Zdorovets, M.V. Synthesis, structural properties and shielding efficiency of glasses based on TeO₂-(1-x)ZnO-xSm₂O₃. *J. Mater. Sci. Mater. Electron.* **2021**, *32*, 12111–12120. [[CrossRef](#)]
9. Almessiere, M.A.; Algarou, N.A.; Slimani, Y.; Sadaqat, A.; Baykal, A.; Manikandan, A.; Trukhanov, S.V.; Trukhanov, A.V.; Ercan, I. Investigation of exchange coupling and microwave properties of hard/soft (SrNi_{0.02}Zr_{0.01}Fe_{11.96}O₁₉)/(CoFe₂O₄)_x nanocomposites. *Mater. Today Nano* **2022**, *18*, 100186. [[CrossRef](#)]
10. Torregrossa, D.; Khoobroo, A.; Fahimi, B. Prediction of Acoustic Noise and Torque Pulsation in PM Synchronous Machines With Static Eccentricity and Partial Demagnetization Using Field Reconstruction Method. *IEEE Trans. Ind. Electron.* **2012**, *59*, 934–944. [[CrossRef](#)]
11. Moon, S.; Lee, J.; Jeong, H.; Kim, S.W. Demagnetization Fault Diagnosis of a PMSM Based on Structure Analysis of Motor Inductance. *IEEE Trans. Ind. Electron.* **2016**, *63*, 3795–3803. [[CrossRef](#)]
12. Skowron, M.; Orłowska-Kowalska, T.; Kowalski, C.T. Detection of Permanent Magnet Damage of PMSM Drive Based on Direct Analysis of the Stator Phase Currents Using Convolutional Neural Network. *IEEE Trans. Ind. Electron.* **2022**, *69*, 13665–13675. [[CrossRef](#)]
13. Moon, S.; Jeong, H.; Lee, H.; Kim, S.W. Detection and Classification of Demagnetization and Interturn Short Faults of IPMSMs. *IEEE Trans. Ind. Electron.* **2017**, *64*, 9433–9441. [[CrossRef](#)]
14. Espinosa, A.G.; Rosero, J.A.; Cusidó, J.; Romeral, L.; Ortega, J.A. Fault Detection by Means of Hilbert–Huang Transform of the Stator Current in a PMSM With Demagnetization. *IEEE Trans. Energy Convers.* **2010**, *25*, 312–318. [[CrossRef](#)]
15. Hong, J.; Hyun, D.; Lee, S.B.; Yoo, J.Y.; Lee, K.W. Automated Monitoring of Magnet Quality for Permanent-Magnet Synchronous Motors at Standstill. *IEEE Trans. Ind. Appl.* **2010**, *46*, 1397–1405. [[CrossRef](#)]
16. Brella, M.; Michalski, M.; Gebhardt, H.J.; Franke, J. Hall measurement method for the detection of material defects in plastic-embedded permanent magnets of rotors. In Proceedings of the IECON 2013—39th Annual Conference of the IEEE Industrial Electronics Society, Vienna, Austria, 10–13 November 2013; pp. 3928–3934.
17. Roux, W.L.; Harley, R.G.; Habetler, T.G. Detecting Rotor Faults in Low Power Permanent Magnet Synchronous Machines. *IEEE Trans. Power Electron.* **2007**, *22*, 322–328. [[CrossRef](#)]
18. Chakraborty, S.; Keller, E.; Ray, A.; Mayer, J. Detection and estimation of demagnetization faults in permanent magnet synchronous motors. *Electr. Power Syst. Res.* **2013**, *96*, 225–236. [[CrossRef](#)]
19. Rajagopalan, S.; Roux, W.L.; Habetler, T.G.; Harley, R.G. Dynamic Eccentricity and Demagnetized Rotor Magnet Detection in Trapezoidal Flux (Brushless DC) Motors Operating Under Different Load Conditions. *IEEE Trans. Power Electron.* **2007**, *22*, 2061–2069. [[CrossRef](#)]
20. Khoobroo, A.; Fahimi, B. A novel method for permanent magnet demagnetization fault detection and treatment in permanent magnet synchronous machines. In Proceedings of the 2010 Twenty-Fifth Annual IEEE Applied Power Electronics Conference and Exposition (APEC), Palm Springs, CA, USA, 21–25 February 2010; pp. 2231–2237.
21. Kliman, G.B.; Stein, J. Methods of Motor Current Signature Analysis. *Electr. Mach. Power Syst.* **1992**, *20*, 463–474. [[CrossRef](#)]
22. Thomson, W.T.; Fenger, M. Current signature analysis to detect induction motor faults. *IEEE Ind. Appl. Mag.* **2001**, *7*, 26–34. [[CrossRef](#)]
23. Zafarani, M.; Goktas, T.; Akin, B. A comprehensive analysis of magnet defect faults in permanent magnet synchronous motors. In Proceedings of the 2015 IEEE Applied Power Electronics Conference and Exposition (APEC), Long Beach, CA, USA, 15–19 March 2015; pp. 2779–2783.
24. Goktas, T.; Zafarani, M.; Akin, B. Discernment of Broken Magnet and Static Eccentricity Faults in Permanent Magnet Synchronous Motors. *IEEE Trans. Energy Convers.* **2016**, *31*, 578–587. [[CrossRef](#)]

25. Rajagopalan, S.; Aller, J.M.; Restrepo, J.A.; Habetler, T.G.; Harley, R.G. Detection of Rotor Faults in Brushless DC Motors Operating Under Nonstationary Conditions. *IEEE Trans. Ind. Appl.* **2006**, *42*, 1464–1477.
26. Rajagopalan, S.; Aller, J.M.; Restrepo, J.A.; Habetler, T.G.; Harley, R.G. Analytic-Wavelet-Ridge-Based Detection of Dynamic Eccentricity in Brushless Direct Current (BLDC) Motors Functioning Under Dynamic Operating Conditions. *IEEE Trans. Ind. Electron.* **2007**, *54*, 1410–1419. [[CrossRef](#)]
27. Ruiz, J.R.; Rosero, J.A.; Espinosa, A.G.; Romeral, L. Detection of Demagnetization Faults in Permanent-Magnet Synchronous Motors Under Nonstationary Conditions. *IEEE Trans. Magn.* **2009**, *45*, 2961–2969. [[CrossRef](#)]
28. Ruiz, J.R.R.; Espinosa, A.G.; Romeral, L.; Cusidó, J. Demagnetization diagnosis in permanent magnet synchronous motors under non-stationary speed conditions. *Electr. Power Syst. Res.* **2010**, *80*, 1277–1285. [[CrossRef](#)]
29. Urresty, J.; Riba, J.; Delgado, M.; Romeral, L. Detection of Demagnetization Faults in Surface-Mounted Permanent Magnet Synchronous Motors by Means of the Zero-Sequence Voltage Component. *IEEE Trans. Energy Convers.* **2012**, *27*, 42–51. [[CrossRef](#)]
30. Ebrahimi, B.M.; Faiz, J. Demagnetization Fault Diagnosis in Surface Mounted Permanent Magnet Synchronous Motors. *IEEE Trans. Magn.* **2013**, *49*, 1185–1192. [[CrossRef](#)]
31. Urresty, J.; Atashkhouei, R.; Riba, J.; Romeral, L.; Royo, S. Shaft Trajectory Analysis in a Partially Demagnetized Permanent-Magnet Synchronous Motor. *IEEE Trans. Ind. Electron.* **2013**, *60*, 3454–3461. [[CrossRef](#)]
32. Yang, Z.; Shi, X.; Krishnamurthy, M. Vibration monitoring of PM synchronous machine with partial demagnetization and inter-turn short circuit faults. In Proceedings of the 2014 IEEE Transportation Electrification Conference and Expo (ITEC), Dearborn, MI, USA, 15–18 June 2014; pp. 1–6.
33. Rezig, A.; Mekideche, M.R.; Djerdir, A. Impact of Eccentricity and Demagnetization Faults on Magnetic Noise Generation in Brushless Permanent Magnet DC Motors. *J. Electr. Eng. Technol.* **2011**, *6*, 356–363. [[CrossRef](#)]
34. Hong, J.; Park, S.; Hyun, D.; Kang, T.; Lee, S.B.; Kral, C.; Haumer, A. Detection and Classification of Rotor Demagnetization and Eccentricity Faults for PM Synchronous Motors. *IEEE Trans. Ind. Appl.* **2012**, *48*, 923–932. [[CrossRef](#)]
35. Eker, M.; Gündogan, B. Demagnetization fault detection of permanent magnet synchronous motor with convolutional neural network. *Electr. Eng.* **2023**, *105*, 1695–1708. [[CrossRef](#)]
36. Zeng, C.; Huang, S.; Lei, J.; Wan, Z.; Yang, Y. Online Rotor Fault Diagnosis of Permanent Magnet Synchronous Motors Based on Stator Tooth Flux. *IEEE Trans. Ind. Appl.* **2021**, *57*, 2366–2377. [[CrossRef](#)]
37. Da, Y.; Shi, X.; Krishnamurthy, M. A New Approach to Fault Diagnostics for Permanent Magnet Synchronous Machines Using Electromagnetic Signature Analysis. *IEEE Trans. Power Electron.* **2013**, *28*, 4104–4112. [[CrossRef](#)]
38. Driscoll, T.A.; Trefethen, L.N. *Schwarz-Christoffel Mapping*; Cambridge University Press: Cambridge, UK, 2002.
39. Park, Y.; Fernandez, D.; Lee, S.B.; Hyun, D.; Jeong, M.; Kommuri, S.K.; Cho, C.; Reigosa, D.D.; Briz, F. Online Detection of Rotor Eccentricity and Demagnetization Faults in PMSMs Based on Hall-Effect Field Sensor Measurements. *IEEE Trans. Ind. Appl.* **2019**, *55*, 2499–2509. [[CrossRef](#)]
40. Fernandez, D.; Hyun, D.; Park, Y.; Reigosa, D.D.; Lee, S.B.; Lee, D.M.; Briz, F. Permanent Magnet Temperature Estimation in PM Synchronous Motors Using Low-Cost Hall Effect Sensors. *IEEE Trans. Ind. Appl.* **2017**, *53*, 4515–4525. [[CrossRef](#)]
41. Reigosa, D.; Fernández, D.; Martínez, M.; Park, Y.; Lee, S.B.; Briz, F. Permanent Magnet Synchronous Machine Non-Uniform Demagnetization Detection Using Zero-Sequence Magnetic Field Density. *IEEE Trans. Ind. Appl.* **2019**, *55*, 3823–3833. [[CrossRef](#)]
42. Jeong, J.; Lee, H.; Orviz, M.; Lee, S.B.; Reigosa, D.; Briz, F. Detection of Trailing Edge PM Demagnetization in Surface PM Synchronous Motors. *IEEE Trans. Ind. Appl.* **2023**, *59*, 3390–3399. [[CrossRef](#)]
43. Ahsanullah, K.; Jeyasankar, E.; Panda, S.K.; Shanmukha, R.; Nadarajan, S. Detection and analysis of winding and demagnetization faults in PMSM based marine propulsion motors. In Proceedings of the 2017 IEEE International Electric Machines and Drives Conference (IEMDC), Miami, FL, USA, 21–24 May 2017; pp. 1–7.

Disclaimer/Publisher’s Note: The statements, opinions and data contained in all publications are solely those of the individual author(s) and contributor(s) and not of MDPI and/or the editor(s). MDPI and/or the editor(s) disclaim responsibility for any injury to people or property resulting from any ideas, methods, instructions or products referred to in the content.